

Band gap, electronic structure, and surface electron accumulation of cubic and rhombohedral In_2O_3

P. D. C. King,^{1,*} T. D. Veal,¹ F. Fuchs,² Ch. Y. Wang,³ D. J. Payne,⁴ A. Bourlange,⁴ H. Zhang,⁴ G. R. Bell,¹ V. Cimalla,³ O. Ambacher,³ R. G. Egdell,⁴ F. Bechstedt,² and C. F. McConville^{1,†}

¹*Department of Physics, University of Warwick, Coventry CV4 7AL, United Kingdom*

²*Institut für Festkörperteorie und-Optik, Friedrich-Schiller-Universität, Max-Wien-Platz 1, D-07743 Jena, Germany*

³*Fraunhofer-Institut für Angewandte Festkörperphysik, Tullastraße 72, 79108 Freiburg, Germany*

⁴*Department of Chemistry, Chemistry Research Laboratory, University of Oxford, Mansfield Road, Oxford OX1 3TA, United Kingdom*

(Received 26 March 2009; published 29 May 2009)

The bulk and surface electronic structure of In_2O_3 has proved controversial, prompting the current combined experimental and theoretical investigation. The band gap of single-crystalline In_2O_3 is determined as 2.93 ± 0.15 and 3.02 ± 0.15 eV for the cubic bixbyite and rhombohedral polymorphs, respectively. The valence-band density of states is investigated from x-ray photoemission spectroscopy measurements and density-functional theory calculations. These show excellent agreement, supporting the absence of any significant indirect nature of the In_2O_3 band gap. Clear experimental evidence for an s - d coupling between In $4d$ and O $2s$ derived states is also observed. Electron accumulation, recently reported at the (001) surface of bixbyite material, is also shown to be present at the bixbyite (111) surface and the (0001) surface of rhombohedral In_2O_3 .

DOI: [10.1103/PhysRevB.79.205211](https://doi.org/10.1103/PhysRevB.79.205211)

PACS number(s): 78.20.-e, 71.20.Nr, 73.20.-r, 79.60.-i

I. INTRODUCTION

Tin-doped indium oxide is one of the most widely used transparent conducting oxides (TCOs). The unusual combination of optical transparency in the visible region and a high electrical conductivity make it a crucial material in a range of devices including liquid crystal displays and solar cells.^{1,2} Despite this, the basic optoelectronic properties of In_2O_3 have been intensely debated. Its direct band gap was long thought to be ~ 3.75 eV from the onset of significant optical absorption, with a low-intensity onset of absorption below this energy attributed to indirect optical transitions.^{3,4} This indirect band gap hypothesis was not, however, supported by theoretical calculations, which found no significant indirect nature of the band gap.⁵⁻⁹ These experimental and theoretical results have recently been reconciled,^{8,9} with In_2O_3 shown to have a direct band gap $E_g \lesssim 3$ eV. The weak nature of optical absorption around this energy can be attributed to transitions between the highest valence-band states and states at the conduction-band minimum (CBM) being dipole forbidden or having only minimal dipole intensity. The surface electronic properties of In_2O_3 have also proved controversial. A pronounced depletion of carriers has previously been reported at the surface of In_2O_3 .^{10,11} However, investigations of high-quality single-crystalline material have recently shown an accumulation of electrons occurs at the (001) surface,¹² as for the similar TCO compound, CdO,¹³ and the other In-containing compounds, InN (Ref. 14) and InAs.¹⁵

Following recent efforts in growth, it is now possible to obtain high-quality single-crystalline In_2O_3 in the stable body centered cubic (bcc) bixbyite structure by both metal-organic chemical-vapor deposition (MOCVD) and oxygen plasma-assisted molecular-beam epitaxy (PAMBE).^{16,17} Despite the tendency for In_2O_3 to be heavily n -type, almost nondegenerate films have now been achieved.¹² In addition, by judicious choice of substrate, growth temperature and tri-

methylindium flow rate during MOCVD, growth of the metastable rhombohedral (rh) phase of In_2O_3 has been demonstrated.¹⁸ Recent work has suggested enormous potential for the use of TCO materials as the active layers in electronic and short wavelength optoelectronic devices, rather than just their use as transparent contacts.¹⁹⁻²³ In order to probe the potential of In_2O_3 for such applications, it is necessary to investigate the electronic structure and properties of both bcc and rh high-quality single-crystalline In_2O_3 samples, rather than the often polycrystalline, highly defective samples produced by methods such as magnetron sputtering, evaporation, or by pressing pellets of In_2O_3 powder, which have been the subject of the majority of prior investigations.^{1,4,10,11,24,25} Such an investigation into the band gap, valence electronic structure, and surface electronic properties, combining experimental and theoretical studies, is presented here.

II. EXPERIMENTAL AND THEORETICAL DETAILS

Optical absorption spectroscopy measurements were performed using a Perkin-Elmer Lambda 25 and a Varian Cary 5000 UV-visible spectrophotometer. Infrared (IR) reflectivity measurements were performed using a Perkin-Elmer Spectrum GX Fourier transform infrared spectrometer, using a specular scattering geometry at a 35° angle to the surface normal. The spectra were referenced to the reflectivity from an optical mirror. Single-field Hall effect measurements were performed in the Van der Pauw geometry. High-resolution x-ray photoemission spectroscopy (XPS) measurements were performed using a Scienta ESCA300 spectrometer at the National Centre for Electron Spectroscopy and Surface Analysis, Daresbury Laboratory, UK. X-rays, of energy $h\nu = 1486.6$ eV, were produced using a monochromated rotating anode Al $K\alpha$ x-ray source. The ejected photoelectrons were analyzed by a 300 mm mean radius spherical-sector

electron energy analyzer with 0.8 mm slits at a pass energy of 150 eV. The effective instrumental resolution, determined by fitting a broadened Fermi function to the Fermi edge of an ion-bombarded silver reference sample, is 0.4 eV due to the Gaussian convolution of the analyzer broadening and the natural linewidth of the x-ray source (0.27 eV). All measurements were performed at room temperature.

Density-functional theory (DFT) calculations were performed using the Vienna *ab initio* simulation package, treating electron-ion interactions within the projector-augmented wave method. For the calculations of the electronic density of states (DOS), the hybrid functional HSE03 was employed to account for exchange and correlation.²⁶ For comparison with the photoemission measurements, the calculated DOS was convolved with a 0.4 eV full width at half maximum (FWHM) Gaussian and a 0.4 eV FWHM Lorentzian to account for instrumental and lifetime broadening, respectively. For the rh polymorph, the theoretical band gap was calculated by employing G_0W_0 quasiparticle (QP) corrections of the HSE03 eigenvalues. However, the large size of the unit cell made this method too computationally expensive for the bcc-In₂O₃ polymorph. Consequently, the gap opening caused by QP corrections for the rh polymorph was applied as a rigid shift for the bcc polymorph, therefore approximately including QP effects. The spectral shape of the DOS is very similar between the HSE03 results and those incorporating QP corrections,⁹ although the position of the In 4*d* derived bands is shifted to slightly higher binding energy by the QP corrections. Optical spectra were calculated from the band structure determined within the local-density approximation, treated within the independent QP approximation using scissor shifts to correct the band gap to that obtained from the HSE+QP calculations. Further details of the calculations are described elsewhere.⁹

Single-crystalline epitaxial thin films of In₂O₃ (ranging in thickness from ~50 to ~500 nm) were investigated here. bcc-In₂O₃(111) was grown by MOCVD at 400 °C on a sapphire(0001) substrate incorporating InN, GaN, and AlN buffer layers and by PAMBE on a yttria-stabilized cubic-zirconia (YSZ) (111) substrate at 650 °C. bcc-In₂O₃(001) was grown by PAMBE at 650 °C on a YSZ(001) substrate. rh-In₂O₃(0001) was grown by MOCVD at 600 °C on a sapphire(0001) substrate. This film was estimated to contain less than 10% cubic inclusions. Further details of the growth and structural characterization are reported elsewhere.^{16–18} The carrier density (mobility) of the samples were determined from single-field Hall effect measurements to be $1.5 \times 10^{18} \text{ cm}^{-3}$ ($11 \text{ cm}^2 \text{ V}^{-1} \text{ s}^{-1}$) for the MBE bcc-(111) sample, $7.5 \times 10^{18} \text{ cm}^{-3}$ ($32 \text{ cm}^2 \text{ V}^{-1} \text{ s}^{-1}$) for the MBE bcc-(001) sample, and $6.2 \times 10^{18} \text{ cm}^{-3}$ ($55 \text{ cm}^2 \text{ V}^{-1} \text{ s}^{-1}$) for the MOCVD rh-(0001) sample. Example IR reflectivity spectra from the bcc-(111) and rh-(0001) samples are shown in Fig. 1. The carrier concentrations of the samples determined from single-field Hall effect results are in good agreement with the plasma frequency determined from simulation of the IR reflectivity spectra using the method described in Ref. 27 but additionally including incoherent reflections from the rear face of the substrate in the dielectric theory simulations. Due to the conducting buffer layer structure employed, single-field Hall effect results could not be used to determine the

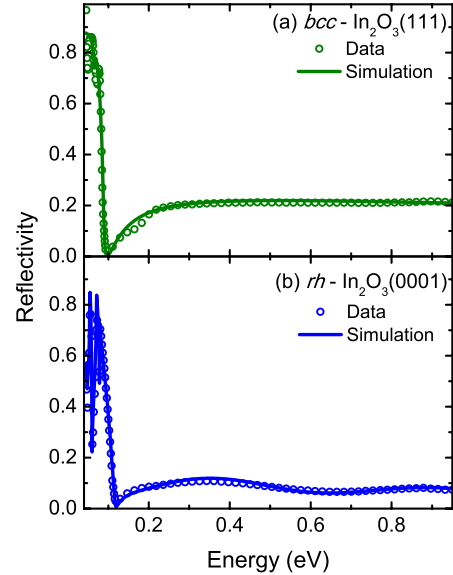


FIG. 1. (Color online) Measured IR reflectivity spectra (points) and dielectric theory simulations (lines) of (a) bcc-In₂O₃(111) grown by PAMBE, and (b) rh-In₂O₃(0001) grown by MOCVD.

carrier density in the MOCVD bcc-(111) sample. However, from the simulation of IR reflectivity measurements for this sample, the carrier density was estimated to be $2.0 \times 10^{19} \text{ cm}^{-3}$.

III. BAND GAP

The measured optical absorption coefficient from bcc-In₂O₃ is shown in Fig. 2(a). Significant onset of absorption in the measured spectrum occurs above ~3.5 eV, broadly consistent with previous observations.^{3,18} A pro-

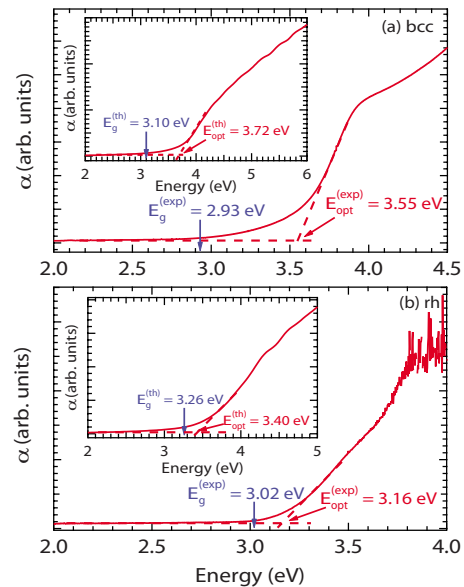


FIG. 2. (Color online) Experimental absorption coefficient, α , measured from (a) bcc-In₂O₃(001) and (b) rh-In₂O₃(0001). The calculated absorption coefficient for each polymorph is shown inset.

nounced low-energy tail is seen below this absorption edge. In previous reports, this was attributed to indirect optical absorption,³ in contrast to the results of theoretical band-structure calculations.^{5–7} However, as discussed in the introduction, an alternative explanation has recently emerged.^{8,9} Walsh *et al.*⁸ and Fuchs and Bechstedt⁹ showed that, due to the symmetry of the bixbyite crystal structure, optical transitions from the valence-band maximum (VBM) to the CBM are forbidden within the dipole approximation. Furthermore, transitions from the valence bands somewhat below the VBM to the conduction band are also either forbidden or have only very weak optical transition matrix elements. The result is evident in the calculated optical absorption spectrum, shown inset in Fig. 2(a), where a significant increase in the absorption coefficient is only observed at energies ~ 0.5 – 1 eV above the fundamental band gap.

Consequently, experimental investigations have consistently reported a band gap of bcc-In₂O₃ that is significantly too high. Here, we define the “optical gap” as the energy corresponding to the onset of significant optical absorption. This is determined by extrapolating the leading ledge of the optical absorption coefficient, α , to the baseline, as shown in Fig. 2(a), giving a value of $E_{\text{opt}}^{(\text{exp})} = 3.55 \pm 0.05$ eV for the experimentally determined room-temperature optical gap of the bcc polymorph. This is slightly lower than the value of ≥ 3.7 eV typically reported in previous studies. This difference is attributed largely to the different methods of analysis used in various cases. For example, performing, as is often done, an extrapolation of the square of the absorption coefficient for this sample to the baseline (not shown) gives a value of 3.68 ± 0.05 eV, in approximate agreement with the lower limit of frequently determined values for the In₂O₃ optical gap. However, as this absorption onset is not due to interband transitions around the band extrema, there is no justification for using an α^2 extrapolation in this case and we choose to define the onset of significant absorption based on the actual absorption coefficient, as described above. It is also necessary to point out that, from carrier statistics calculations including a nonparabolic conduction-band dispersion, the Fermi level was estimated to lie only 0.02 eV above the CBM in this sample, in contrast to the often highly degenerate nature of this material. Consequently, the Moss-Burstein effect,^{28,29} which causes a shift of the onset of optical absorption to higher energies due to band filling, can be neglected here. This was not the case in all previous studies.

The same analysis was applied to the calculated absorption spectrum, shown inset in Fig. 2(a), giving an optical gap of $E_{\text{opt}}^{(\text{th})} = 3.72 \pm 0.10$ eV, slightly higher than the measured optical gap. This difference could result from the effects of the band gap reduction with increasing temperature, as discussed below, and also errors in the calculated value of the band gap. However, the band-gap determination performed here is not sensitive to these shifts. The theoretical optical gap lies 0.62 eV above the calculated fundamental band gap of $E_g^{(\text{th})} = 3.10$ eV, indicating the effects of crystal symmetry on the dipole transition matrix elements discussed above. Applying the same difference between the optical and fundamental energy gaps for the experimental results, this allows the fundamental energy gap of bcc-In₂O₃ to be estimated as $E_g^{(\text{exp})} = 2.93 \pm 0.15$ eV. Note, Walsh *et al.*⁸ recently

reported that the onset of optical absorption does not occur until energies 0.81 eV above the fundamental band gap, suggesting a slightly larger shift between the fundamental and optical band gaps than determined here. However, lifetime broadening was not applied in the optical absorption coefficient calculations of Walsh *et al.*,⁸ as was included here, which decreases the value of the optical gap slightly. Consequently, a similar shift between the fundamental band gap and the onset of optical absorption as that determined here would be expected.

The following points should be noted about this determination. First, due to the complexity of this system, the theoretical calculations of the absorption coefficient do not include QP effects, besides a rigid gap opening, or excitonic effects. While the experimental spectra do not show any indications of bound excitons, these effects could still cause a slight redshift of the absorption edge. In contrast, QP effects would tend to cause a slight “stretching” of the conduction and valence-band electronic structure around the band gap,⁹ leading to a slight blueshift of the absorption edge. The combination of these effects lead to some uncertainty in the determined fundamental band gap, as represented by the error given on this quantity. Additionally, the calculations are for a zero temperature limit, whereas the measurements were performed at room temperature. Broadening of the spectral features due to lifetime effects has been included in the calculations, but the band gap of semiconductors is also known to reduce in size with increasing temperature due to a mixture of lattice dilation effects and electron-phonon interactions.³⁰ Indeed, for the similar material SnO₂, the shift of the band gap between 0 K and room temperature is ~ 0.2 eV.³¹ Such a shift is not included in the independent QP approximation used to correct the band gap for calculating the theoretical absorption coefficient here. The above treatment, however, is not sensitive to the exact calculated band-gap value; rather the comparison of the experiment with the theoretical calculations serves to account for the variation in the transition matrix elements on the onset of optical absorption. The determination of the room-temperature band gap would therefore still be expected to hold. Indeed, the experimental value determined here being slightly lower than the calculated fundamental band gap is consistent with a reduction in band gap with increasing temperature.

The fundamental band gap determined here is slightly higher than the weak onset of absorption identified by Weiher and Ley³ as due to indirect transitions, but which can now be understood as due to dipole forbidden or minimal dipole intensity transitions. However, Weiher and Ley analyzed this absorption edge assuming that it had the spectral shape associated with indirect transitions in a parabolic band semiconductor—both of these assumptions are not true for this absorption in In₂O₃, which could lead to significant inaccuracies in the extrapolated value for the onset of absorption. Also, the effects of Urbach tailing and lifetime broadening on this absorption onset, which could cause a pronounced shift between the extrapolated onset of such a weak absorption feature and the fundamental band gap, were not considered. These effects would lead to optical absorption at lower energies than would be expected from the band structure alone, further explaining why the weak onset of

optical absorption determined previously is below the fundamental band gap value determined here. For degenerate samples with a high concentrations of free electrons ($\sim 10^{20}$ – 10^{21} cm $^{-3}$) the weak absorption onset at low energies (~ 2.6 eV) observed previously has also been attributed to interconduction-band transitions, as discussed in Ref. 9, providing a further possible mechanism to explain differences with some previous results.

The equivalent investigation for rh-In $_2$ O $_3$ was also performed, as shown in Fig. 2(b). While the rh structure does not result in symmetry forbidden optical transitions around the band gap, the DOS close to the bottom of the conduction band is very small and the conduction-band dispersion is nonparabolic,⁹ resulting in a more gradual onset of optical absorption than would be expected for a conventional direct band gap semiconductor characterized by parabolic dispersion relations. Indeed, performing the same analysis as for the bcc case discussed above, the optical gap is determined from the calculated absorption coefficient as $E_{\text{opt}}^{(\text{th})} = 3.40 \pm 0.10$ eV, 0.14 eV above the calculated fundamental band gap value of $E_g^{(\text{th})} = 3.26$ eV. Consequently, the experimentally observed optical gap of $E_{\text{opt}}^{(\text{exp})} = 3.16 \pm 0.05$ eV suggests a fundamental band gap of $E_g^{(\text{exp})} = 3.02 \pm 0.15$ eV, in reasonable agreement with previous studies.¹⁸ Despite the large differences in the optical gap, the fundamental band gaps of bcc- and rh-In $_2$ O $_3$ are therefore rather similar, consistent with theoretical predictions.⁹

IV. VALENCE-BAND DENSITY OF STATES

The above results are dependent on the valence electronic structure of the material. To support these, it is necessary to compare the results of valence electronic structure calculations to directly measurable physical properties which do not suffer from the same ambiguities as the optical spectra. This is achieved here by a comparison of valence-band photoemission spectra with calculations of the valence-band DOS (VB-DOS). XPS measurements are particularly suited to such a study due to the full Brillouin-zone sampling and negligible structure introduced by final-state effects on the photoemission intensity. Valence-band XPS measurements therefore effectively give the total VB-DOS, as has previously been confirmed both for metals³² and for a variety of III-V and II-VI semiconductors.^{33–36}

Shirley-background-subtracted valence-band photoemission from bcc-In $_2$ O $_3$ (111) is shown in Fig. 3(a). Also shown is the calculated VB-DOS, with and without lifetime and instrumental broadening. The calculated VB-DOS exhibits a large number of narrow peaks, due to the large numbers of valence bands and their limited dispersions, shown in Fig. 3(b). However, when lifetime and instrumental broadening are applied, these narrow peaks merge together. The resulting VB-DOS is rather more complex than the characteristic “two-peak” structure of other semiconductors,³⁴ including other metal oxides.³⁶ Of particular note is the very shallow dispersion of the topmost valence band. In fact, an indirect gap is predicted by the calculations, with the VBM slightly away from Γ in the Γ - H direction. However, the energy of the valence band at Γ is only ~ 50 meV below the VBM,

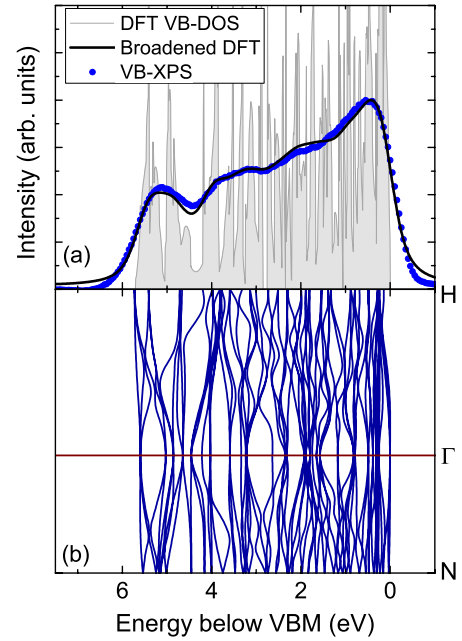


FIG. 3. (Color online) (a) Shirley-background-subtracted valence-band photoemission spectrum and DFT VB-DOS calculations shown without (shaded) and with lifetime and instrumental broadening for bcc-In $_2$ O $_3$ (111). The measured valence-band photoemission is rigidly shifted to lower energies by 3.4 eV to align the VBM at 0 eV binding energy as for the calculations. The XPS and DFT spectra are normalized to the same maximum peak intensity. The corresponding DFT valence-band-structure calculations for bcc-In $_2$ O $_3$ are shown in (b).

and so this is not a significant effect. The shallow dispersion of the top valence band leads to a very sharp onset of the VB-DOS, although this is considerably less steep in the experimental spectrum due to the effects of lifetime and instrumental broadening. The same is true for the bottom of the VB-DOS.

The experimental spectrum has been rigidly shifted to lower binding energies by 3.4 eV to align the Fermi level at the VBM, as for the theoretical calculations. This is discussed further in Sec. VI. Following this shift, both the energetic positions and relative intensities of the local maxima and minima in the broadened VB-DOS calculations show excellent agreement with the measured photoemission spectrum. This gives confidence in the band gap determination performed above, which depends on the calculated properties of the valence bands. The excellent agreement between theory and experiment also gives confidence that there is negligible indirect nature of the bcc-In $_2$ O $_3$ band gap.

Previous soft-x-ray emission (SXE) measurements of In $_2$ O $_3$ show much more spectral weight close to the top of the VBM than in the XPS results presented here.²⁵ The SXE measurements probed the O 2*p* partial DOS (PDOS), whereas XPS effectively probes the total VB-DOS. Consequently, this indicates that the valence band is dominated by O 2*p* states close to the VBM, but has appreciable mixing of other orbital character away from the VBM. This is confirmed by calculations of the PDOS, shown in Fig. 4(b), which indicate considerable *s*-orbital character close to the

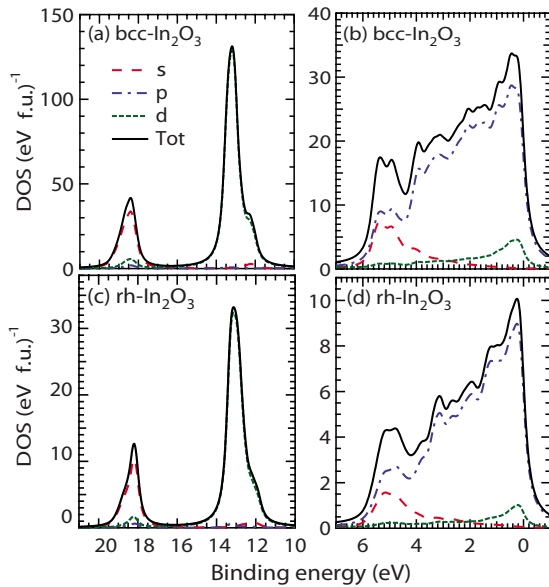


FIG. 4. (Color online) DFT PDOS calculations for [(a) and (b)] bcc- and [(c) and (d)] rh- In_2O_3 around the valence bands [(b) and (d)] and In $4d$ levels [(a) and (c)]. The PDOS is resolved into s , p , and d components. The total DOS is also shown. The calculations have been convolved with a 0.4 eV FWHM lorentzian to account for lifetime broadening.

bottom of the valence bands. Additionally, some In $4d$ orbital character is seen close to the VBM, due to the effects of hybridization between O $2p$ and In $4d$ states. The In $4d$ -derived states will be discussed in further detail in Sec. V.

The equivalent investigation of the valence electronic structure of rh- In_2O_3 has also been performed here. The Shirley-background-subtracted valence-band photoemission measurements and broadened and unbroadened VB-DOS calculations are shown in Fig. 5(a). The unit cell for the rh polymorph contains only 30 atoms, rather than the 80 atoms of the bcc unit cell. Consequently, the valence-band structure is rather simpler than for the bcc case, as shown in Fig. 5(b), although the situation is complicated somewhat in this case by the anisotropy of the rh crystal structure. The valence bands disperse more than for the bcc polymorph, causing the VB-DOS to be slightly less sharply peaked in this case. However, when lifetime and instrumental broadening are applied, the resulting VB-DOS is rather similar to that of the bcc polymorph, although the calculations for rh- In_2O_3 contain slightly more spectral weight close to the VBM. The dispersion of the top valence band is still shallow, leading to a very sharp onset of the VB-DOS, as for the bcc polymorph, although this is again broadened significantly by instrumental and lifetime effects.

Following a shift of the experimental spectrum by 3.5 eV to align the Fermi levels in the measurement and calculations, discussed in detail in Sec. VI, the energetic positions of spectral features agree very well between the calculated and measured spectra. However, there are some differences in relative intensity. This might suggest that too much spectral weight results close to the top of the valence band, or too little deeper in the valence band, in the calculations, although

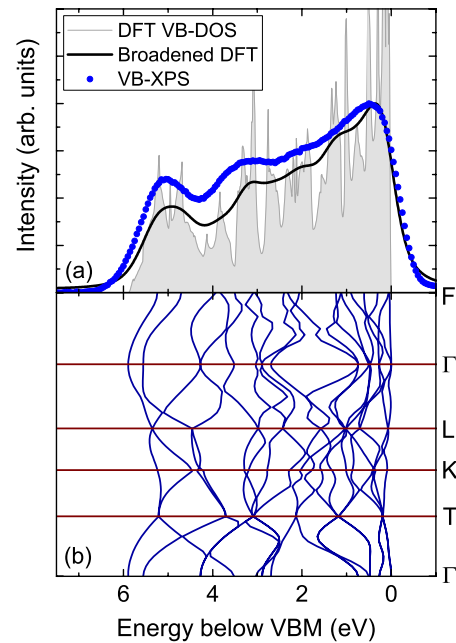


FIG. 5. (Color online) (a) Shirley-background-subtracted valence-band photoemission spectrum and DFT VB-DOS calculations shown without (shaded) and with lifetime and instrumental broadening for rh- $\text{In}_2\text{O}_3(0001)$. The measured valence-band photoemission is rigidly shifted to lower energies by 3.5 eV to align the VBM at 0 eV binding energy as for the calculations. The XPS and DFT spectra are normalized to the same maximum peak intensity. The corresponding DFT valence-band-structure calculations for rh- In_2O_3 are shown in (b).

this may also be affected by cubic inclusions in the rh sample. PDOS calculations, shown in Fig. 4(d), indicate that the valence bands are predominantly of O $2p$ character again, although with some admixture of d orbitals close to the VBM, and s orbitals close to the bottom of the valence band, as for the bcc case.

V. In $4d$ LEVELS AND s - d HYBRIDIZATION

Shallow semicore d levels have a very large influence on the valence bands of semiconductors,³⁷ as discussed in detail for In_2O_3 elsewhere.⁷⁻⁹ It is therefore of interest to investigate the electronic structure around the In $4d$ levels of bcc- and rh- In_2O_3 in detail.

The calculated DOS from this region for bcc- In_2O_3 , both with and without lifetime and instrumental broadening, is shown in Fig. 6(a). The corresponding band-structure calculations are shown in Fig. 6(b). A large number of effectively dispersionless bands are evident between ~ 13 and ~ 13.5 eV below the VBM, which can be associated with localized In $4d$ states. These bands lead to intense, narrow peaks in the DOS, although these are considerably broadened into a single peak and reduced in intensity by lifetime and instrumental effects. In addition, a shoulder on this peak at lower binding energies and an additional peak at higher binding energies are observed in the DOS calculations, which are due to the presence of O $2s$ orbitals. The orbitally resolved

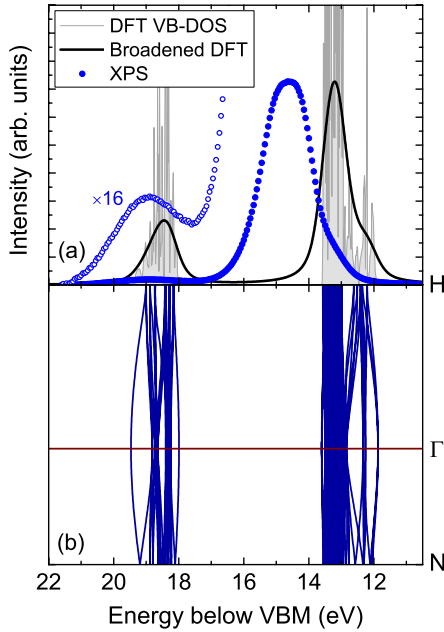


FIG. 6. (Color online) (a) Shirley-background-subtracted photoemission spectrum and corresponding DFT DOS calculations shown without (shaded) and with lifetime and instrumental broadening around the In $4d$ -derived peaks for bcc-In $_2$ O $_3$ (111). The measured photoemission is rigidly shifted to lower energies by 3.4 eV to align the VBM at 0 eV binding energy as for the calculations. The XPS and DFT spectra are normalized to the same maximum peak intensity. The high binding-energy region is also shown magnified $\times 16$. The corresponding DFT band-structure calculations for bcc-In $_2$ O $_3$ are shown in (b).

calculated PDOS for this region is shown in Fig. 4(a). The large peak in the DOS is of almost entirely d -orbital character, deriving from In $4d$ states. The higher binding-energy peak is predominantly of s orbital character, from the O $2s$ states. However, there is also a contribution due to the In $4d$ orbitals. Similarly, the shoulder on the low binding-energy side of the In $4d$ peak, while dominated by its proximity to the In $4d$ levels, also has a component of s orbital character deriving from O $2s$ states. Such an s - d hybridization has previously been predicted for other binary semiconductors where the anion s levels are located at a similar binding energy to cation shallow d levels,³⁸ and has previously been inferred experimentally from photoemission measurements of InN.³⁵ In that case, however, this effect could not be unambiguously determined due to inelastic broadening of the In $4d$ peak.

Shirley-background-subtracted photoemission from bcc-In $_2$ O $_3$ (111) around the In $4d$ peak is also shown in Fig. 6(a). The same 3.4 eV shift in energy has been applied to the experimental spectrum, as for the valence-band photoemission discussed above, to align the Fermi level at 0 eV in both the calculation and experiment. An intense peak, attributed to the In $4d$ levels, is observed in the photoemission measurements, experimentally located at 14.6 ± 0.1 eV below the VBM. This is slightly more bound than in the theoretical calculations; such an underestimation of the d -band binding energy by ~ 1 – 2 eV in DFT calculations employing the HSE03 functional seems to be a rather general feature of this

calculation scheme.³⁹ The measured width of the In $4d$ -like peak is also somewhat larger than that of the broadened calculations. The same broadening has been applied here as for the valence bands. The In $4d$ states are, however, more deeply bound, leading to an increase in lifetime broadening. Such an increase would account for this difference in width between theory and experiment.

A pronounced shoulder is observed on the low binding-energy side of the In $4d$ peak, in good agreement with the d - s hybridized component found in the calculations. As this component has predominantly In $4d$ orbital character, the cross-section for photoemission from this state will be very similar to that of the In $4d$ peaks, giving rise to a good agreement between the relative intensities of the main peak and the shoulder in the experiment and the calculations. In contrast, the s - d hybridized peak in the DOS calculations at ~ 18.5 eV is of predominantly O $2s$ orbital character. The cross-section for photoemission from such a state would be expected to be much lower than from an In $4d$ state and so the corresponding peak observed in the photoemission measurements is of very low intensity, as shown in Fig. 6(a). Indeed, from the photoionization cross section calculations of Yeh and Lindau⁴⁰ and Trzhaskovskaya,⁴¹ the photoemission intensity from In $4d$ states can be estimated to be approximately sixteen times as strong as that from O $2s$ states. Multiplying the photoemission spectrum by this factor, as shown in Fig. 6(a), gives a peak intensity in reasonable agreement with that predicted by the theoretical calculations. Note also that the effects of hybridization with the In $4d$ states, which would be expected to lead to slightly higher intensity than predicted by the simple cross-section arguments employed here, have been neglected. These observations, therefore, present clear experimental evidence for s - d hybridization in the electronic structure of semiconductors.

The equivalent investigation for rh-In $_2$ O $_3$ (0001) is shown in Fig. 7. As for the valence bands, the electronic structure in this region [Fig. 7(b)] is somewhat simpler than for the bcc polymorph, although the DOS [Fig. 7(a)], especially following broadening, is very similar for the two crystal structures. As for the valence-band photoemission, a 3.5 eV shift in energy has been applied to the experimental spectrum to align the Fermi level at 0 eV in both the calculation and experiment. The In $4d$ levels are located at 14.6 ± 0.1 eV, the same as for the bcc polymorph to within the accuracy of the experimental determination, again somewhat more bound than in the calculations. Again, a large d - s hybridized shoulder is observed on the low binding-energy side of the In $4d$ peak, and an s - d hybridized peak is observed at higher binding energies. Multiplying the measured photoemission intensity by a factor of sixteen to account for cross-section variations for photoemission from In $4d$ and O $2s$ states gives good agreement with the theoretical intensity of this component in the DOS.

VI. SURFACE ELECTRON ACCUMULATION

The valence-band photoemission spectra from bcc-In $_2$ O $_3$ (111) and (001) samples, and rh-In $_2$ O $_3$ (0001) are shown in Fig. 8. A magnification of the low binding-energy

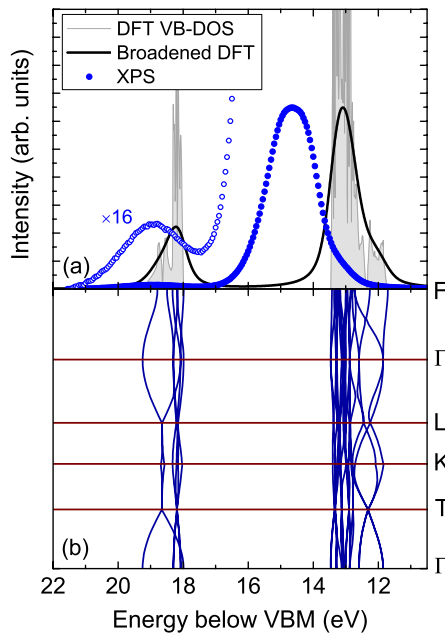


FIG. 7. (Color online) (a) Shirley-background-subtracted photoemission spectrum and corresponding DFT DOS calculations shown without (shaded) and with lifetime and instrumental broadening around the In $4d$ -derived peaks for rh-In $_2$ O $_3$ (0001). The measured photoemission is rigidly shifted to lower energies by 3.5 eV to align the VBM at 0 eV binding energy as for the calculations. The XPS and DFT spectra are normalized to the same maximum peak intensity. The high binding-energy region is also shown magnified $\times 16$. The corresponding DFT band-structure calculations for rh-In $_2$ O $_3$ are shown in (b).

region is also shown. The intensity observed in this region, above the VBM, has previously been attributed to emission from bulk conduction-band states.⁸ However, the samples investigated here are all nearly, or in fact are, nondegenerate in the bulk, from nonparabolic carrier statistics calculations for the measured bulk carrier densities. It is therefore likely that there would be insufficient density of filled conduction-band states in the bulk alone to give rise to such a feature in the photoemission spectra. Further, XPS is a surface sensitive technique, and so this conduction-band emission would not likely be visible if a pronounced depletion of carriers is present at the surface, as suggested in previous reports.^{10,11} If, however, the carrier density at the surface is higher than in the bulk, a peak would be expected in the photoemission spectra, as observed here, corresponding to conduction-band emission from the near-surface region. This supports the recent report¹² of an electron accumulation at bcc-In $_2$ O $_3$ (001) surfaces, and provides initial evidence that the same phenomenon occurs at the surface of bcc-In $_2$ O $_3$ (111) and rh-In $_2$ O $_3$ (0001). Indeed, a recent comparison of the conduction-band emission intensity observed in XPS measurements, using 1486.6 eV photons (as here), and high-energy XPS (HXPS), using 6000 eV photons, has been made.⁴² A distinct decrease in the conduction-band emission intensity was seen in HXPS as compared to XPS measurements. As HXPS measurements have a much larger probing depth than XPS measurements, this supports the conclusion that the high carrier-densities giving rise to the conduction-

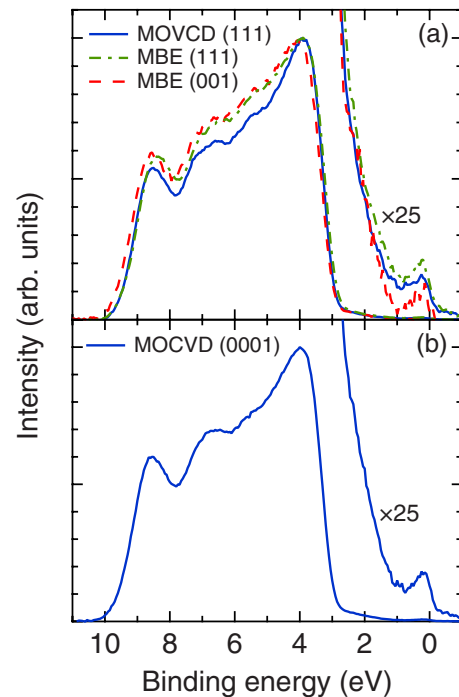


FIG. 8. (Color online) Shirley-background-subtracted valence-band photoemission spectra from (a) bcc-In $_2$ O $_3$ (001) [Ref. 12] and (111) (grown by PAMBE and MOCVD) and (b) rh-In $_2$ O $_3$ (0001). Conduction-band emission can be seen in the spectra, magnified $\times 25$.

band emission are localized near to the surface of the semiconductor, supporting the conclusion of electron accumulation at the surface of In $_2$ O $_3$.

The zero of the binding-energy scale of the measured spectra is referenced to the Fermi level. However, due to the surface specificity of the technique, the reference is the Fermi level at the surface of the semiconductor. Consequently, the photoemission measurements can be used to directly determine the VBM to surface Fermi level separation in this material, as has been performed in a number of previous investigations.^{8,10-12} In these previous investigations, the position of the VBM was determined by a linear extrapolation of the leading edge of the valence-band photoemission to the baseline, to take account of the finite instrumental resolution of the spectrometer.⁴³ However, as discussed in Sec. IV and evident in Figs. 3(a) and 5(a), the shallow dispersion of the top valence band leads to an almost vertical onset of the VB-DOS. Lifetime and instrumental broadening cause the measured onset of the valence-band photoemission to have a significant slope. Extrapolating even over the most linear portion of this slope will cause a large underestimation in the VBM to surface Fermi level separation.

Consequently, a more accurate determination of the VBM to surface Fermi level separation can be obtained by comparisons of the positions of spectral features with those of a calculated VB-DOS which has been suitably broadened. This is true provided that good agreement can be achieved between the photoemission spectrum and the calculated VB-DOS with only a rigid shift of the binding-energy scale to account for Fermi level differences. This was seen to hold

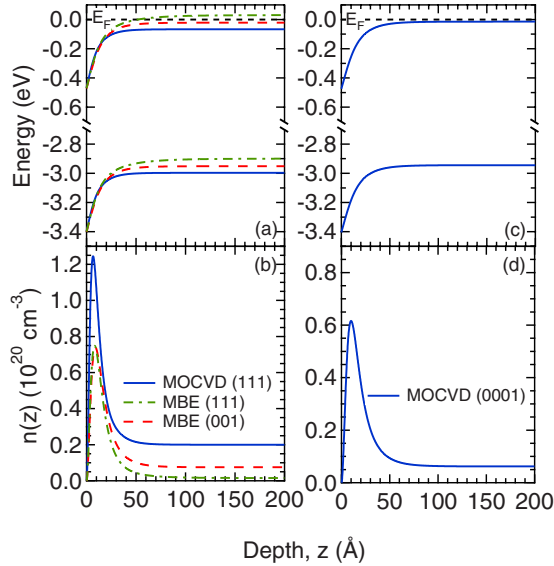


FIG. 9. (Color online) Poisson-MTFA calculations of [(a) and (c)] band bending, and [(b) and (d)] carrier concentration profiles in the electron accumulation layer at the surface of [(a) and (b)] $\text{bcc-In}_2\text{O}_3$ and [(c) and (d)] $\text{rh-In}_2\text{O}_3$.

here, as discussed in Sec. IV. Consequently, the Fermi level is pinned 3.40 ± 0.05 eV above the VBM in the MOCVD $\text{bcc-In}_2\text{O}_3(111)$ sample investigated above. For the measured bulk carrier density, nonparabolic carrier statistics calculations⁴⁴ assuming a band edge electron effective mass of $0.35m_0$,¹ give a bulk Fermi level 0.07 eV above the CBM in this sample, which, taking the band gap of 2.93 eV determined above, lies 3.0 eV above the VBM. Consequently, there is a downward band bending of 0.40 ± 0.16 eV relative to the Fermi level at the surface of the semiconductor. This causes electrons to accumulate at the (111) surface of In_2O_3 , as recently reported for the (001) surface.¹² Valence-band photoemission from a $\text{bcc-In}_2\text{O}_3$ sample grown by PAMBE is very similar to that from the MOCVD sample, revealing a downward band bending of 0.50 ± 0.16 eV from the same method of analysis. This is slightly larger than for the MOCVD sample due to the lower carrier density, but confirms that electron accumulation is an intrinsic property of the material, and not just a product of a particular growth technique. In addition, the valence-band photoemission spectrum of a $\text{bcc-In}_2\text{O}_3(001)$ sample considered previously¹² can be seen, from Fig. 8(a), to occur almost coincident in energy with the $\text{bcc-In}_2\text{O}_3(111)$ samples, leading to a downward band bending of 0.45 ± 0.16 eV. This is slightly larger than the value reported previously¹² due to the alternative method of analysis presented here.

The band bending and carrier-concentration profiles as a function of depth below the surface have been calculated by solving Poisson's equation within a modified Thomas-Fermi approximation^{45,46} (MTFA) incorporating a nonparabolic conduction-band dispersion, as described in detail elsewhere.⁴⁴ These are shown in Figs. 9(a) and 9(b). A pronounced peak in the electron density is observed close to the surface due to the downward band bending. The higher bulk carrier density in the MOCVD (111) sample leads to a

shorter screening length for the accumulation layer, and hence the higher peak electron density seen close to the surface than for the PAMBE-grown samples. This is in spite of the same VBM to surface Fermi level separation in each case.

The origin of the electron accumulation has previously been attributed to the charge neutrality level (CNL) lying well into the conduction band of this material. The surface Fermi level pins below this energy, leading to a positive surface charge associated with unoccupied donor surface states, and hence the electron accumulation.¹² The Poisson-MTFA calculations performed here allow the density of these unoccupied donor surface states to be estimated as $(1.3 \pm 0.1) \times 10^{13} \text{ cm}^{-2}$ for all of the bcc samples. This is again slightly higher than previously reported,¹² due to the alternative method of analysis utilized here. From the analysis of the bulk and surface Fermi level positions in undoped and heavily Sn-doped samples, the CNL was previously located ~ 0.4 eV above the CBM in $\text{bcc-In}_2\text{O}_3$.¹² Reanalyzing this data with the method presented here, the CNL can be estimated as lying ~ 3.6 eV above the VBM, and so consequently ~ 0.65 eV above the CBM, again slightly higher than previously reported.

The Fermi level in the rh sample [Fig. 8(b)] is determined as lying 3.50 ± 0.05 eV above the VBM at the surface, from the comparison with the VB-DOS calculations (Fig. 5). While this is slightly higher above the VBM than for the bcc case, the bulk band gap of the rh polymorph was also determined to be ~ 0.1 eV larger than that of $\text{bcc-In}_2\text{O}_3$ in Sec. III. Consequently, the Fermi level pins at a similar position into the conduction band (0.48 eV above the CBM) in low bulk carrier concentration $\text{rh-In}_2\text{O}_3$ as it does for low bulk carrier concentration $\text{bcc-In}_2\text{O}_3$. The similarity of the bulk band structure of the bcc and rh polymorphs⁹ will result in the CNL lying in a similar location for both cases,¹³ explaining the similar pinning position of the surface Fermi level. This is supported by recent first-principles calculations which locate the CNL 0.54 eV above the CBM in $\text{rh-In}_2\text{O}_3$.⁴⁷ Parameters such as the effective mass are not well known for $\text{rh-In}_2\text{O}_3$. However, using the same ones as for $\text{bcc-In}_2\text{O}_3$ as a first approximation, the bulk Fermi level is determined to lie ~ 0.02 eV above the CBM, leading to a downward band bending of 0.46 ± 0.16 eV and a carrier density profile as shown in Figs. 9(c) and 9(d). This corresponds to a surface state density of $1.2 \times 10^{13} \text{ cm}^{-2}$, similar to that of $\text{bcc-In}_2\text{O}_3$, although these numerical answers should be treated as somewhat approximate. Irrespective of this, however, these results provide clear evidence for an accumulation of electrons at the (0001) surface of $\text{rh-In}_2\text{O}_3$.

VII. CONCLUSIONS

The band gap, valence electronic structure, and surface electronic properties of single-crystalline cubic bixbyite (bcc) and rhombohedral (rh) In_2O_3 have been investigated. From comparisons of theoretical calculations and experimental measurements of the absorption coefficient, the fundamental band gap of bcc- and $\text{rh-In}_2\text{O}_3$ was determined as 2.93 ± 0.15 and 3.02 ± 0.15 eV, respectively. Calculations of

the valence-band density of states were shown to be in excellent agreement with experimental measurements utilizing x-ray photoemission spectroscopy, supporting the lack of any significant indirectness of the band gap of bcc-In₂O₃. Experimental and theoretical evidence for an *s-d* coupling between In 4*d* and O 2*s* states was presented. Comparison of valence-band photoemission with broadened density of states calculations was found to be a more accurate method to determine the surface Fermi level position above the valence-band maximum in this material than the linear extrapolation method commonly applied. Using this method of analysis, electron accumulation was shown to be present at the (111) and (001) surfaces of bcc-In₂O₃ and the (0001) surface of

rh-In₂O₃. The electron accumulation at In₂O₃(001) was shown to be more extreme than previously reported.

ACKNOWLEDGMENTS

D. Law and G. Beamson of NCESS are thanked for assistance with the XPS measurements. We acknowledge the Engineering and Physical Sciences Research Council, U.K., for financial support under Grant Nos. EP/E031595/1 and EP/G004447/1 (Warwick), GR/S94148 (Oxford), and EP/E025722/1 (NCESS), the Deutsche Forschungsgemeinschaft for financial support under Project No. Be1346/20-1, and the BMBF for financial support under Project No. 13N9669.

*philip.d.c.king@physics.org

†c.f.mcconville@warwick.ac.uk

- ¹I. Hamberg and C. G. Granqvist, *J. Appl. Phys.* **60**, R123 (1986).
- ²C. G. Granqvist and A. Hultåker, *Thin Solid Films* **411**, 1 (2002).
- ³R. L. Weiher and R. P. Ley, *J. Appl. Phys.* **37**, 299 (1966).
- ⁴F. Matino, L. Persano, V. Arima, D. Pisignano, R. I. R. Blyth, R. Cingolani, and R. Rinaldi, *Phys. Rev. B* **72**, 085437 (2005).
- ⁵H. Odaka, S. Iwata, N. Taga, S. Ohnishi, Y. Kaneta, and Y. Shigesato, *Jpn. J. Appl. Phys.* **36**, 5551 (1997).
- ⁶O. N. Mryasov and A. J. Freeman, *Phys. Rev. B* **64**, 233111 (2001).
- ⁷P. Erhart, A. Klein, R. G. Egdell, and K. Albe, *Phys. Rev. B* **75**, 153205 (2007).
- ⁸A. Walsh, J. L. F. Da Silva, S. H. Wei, C. Körber, A. Klein, L. F. J. Piper, A. DeMasi, K. E. Smith, G. Panaccione, P. Torelli, D. J. Payne, A. Bourlange, and R. G. Egdell, *Phys. Rev. Lett.* **100**, 167402 (2008).
- ⁹F. Fuchs and F. Bechstedt, *Phys. Rev. B* **77**, 155107 (2008).
- ¹⁰A. Klein, *Appl. Phys. Lett.* **77**, 2009 (2000).
- ¹¹Y. Gassenbauer, R. Schafrank, A. Klein, S. Zafeiratos, M. Hävecker, A. Knop-Gericke, and R. Schlögl, *Phys. Rev. B* **73**, 245312 (2006).
- ¹²P. D. C. King, T. D. Veal, D. J. Payne, A. Bourlange, R. G. Egdell, and C. F. McConville, *Phys. Rev. Lett.* **101**, 116808 (2008).
- ¹³P. D. C. King, T. D. Veal, P. H. Jefferson, J. Zúñiga-Pérez, V. Muñoz-Sanjosé, and C. F. McConville, *Phys. Rev. B* **79**, 035203 (2009).
- ¹⁴I. Mahboob, T. D. Veal, C. F. McConville, H. Lu, and W. J. Schaff, *Phys. Rev. Lett.* **92**, 036804 (2004).
- ¹⁵M. Noguchi, K. Hirakawa, and T. Ikoma, *Phys. Rev. Lett.* **66**, 2243 (1991).
- ¹⁶C. Y. Wang, V. Lebedev, V. Cimalla, T. Kups, K. Tonisch, and O. Ambacher, *Appl. Phys. Lett.* **90**, 221902 (2007).
- ¹⁷A. Bourlange, D. J. Payne, R. G. Egdell, J. S. Foord, P. P. Edwards, M. O. Jones, A. Schertel, P. J. Dobson, and J. L. Hutchison, *Appl. Phys. Lett.* **92**, 092117 (2008).
- ¹⁸C. Y. Wang, V. Cimalla, H. Romanus, T. Kups, G. Ecke, T. Stauden, M. Ali, V. Lebedev, J. Pezoldt, and O. Ambacher, *Appl. Phys. Lett.* **89**, 011904 (2006).
- ¹⁹G. Thomas, *Nature (London)* **389**, 907 (1997).
- ²⁰K. Nomura, H. Ohta, K. Ueda, T. Kamiya, M. Hirano, and H. Hosono, *Science* **300**, 1269 (2003).
- ²¹A. Tsukazaki, A. Ohtomo, T. Onuma, M. Ohtani, T. Makino, M. Sumiya, K. Ohtani, S. F. Chichibu, S. Fuke, Y. Segawa, H. Ohno, H. Koinuma, and M. Kawasakia, *Nature Mater.* **4**, 42 (2005).
- ²²A. Tsukazaki, A. Ohtomo, T. Kita, Y. Ohno, H. Ohno, and M. Kawasaki, *Science* **315**, 1388 (2007).
- ²³A. P. Ramirez, *Science* **315**, 1377 (2007).
- ²⁴C. McGuinness, C. B. Stagarescu, P. J. Ryan, J. E. Downes, D. Fu, K. E. Smith, and R. G. Egdell, *Phys. Rev. B* **68**, 165104 (2003).
- ²⁵L. F. J. Piper, A. DeMasi, S. W. Cho, K. E. Smith, F. Fuchs, F. Bechstedt, C. Körber, A. Klein, D. J. Payne, and R. G. Egdell, *Appl. Phys. Lett.* **94**, 022105 (2009).
- ²⁶J. Heyd, G. E. Scuseria, and M. Ernzerhof, *J. Chem. Phys.* **118**, 8207 (2003).
- ²⁷P. H. Jefferson, S. A. Hatfield, T. D. Veal, P. D. C. King, C. F. McConville, J. Zúñiga-Pérez, and V. Muñoz-Sanjosé, *Appl. Phys. Lett.* **92**, 022101 (2008).
- ²⁸T. S. Moss, *Proc. Phys. Soc. B* **67**, 775 (1954).
- ²⁹E. Burstein, *Phys. Rev.* **93**, 632 (1954).
- ³⁰Y. P. Varshni, *Physica* **34**, 149 (1967).
- ³¹R. Summitt and N. F. Borrelli, *J. Appl. Phys.* **37**, 2200 (1966).
- ³²D. A. Shirley, *Phys. Rev. B* **5**, 4709 (1972).
- ³³R. A. Pollak, L. Ley, S. Kowalczyk, D. A. Shirley, J. D. Joannopoulos, D. J. Chadi, and M. L. Cohen, *Phys. Rev. Lett.* **29**, 1103 (1972).
- ³⁴L. Ley, R. A. Pollak, F. R. McFeely, S. Kowalczyk, and D. A. Shirley, *Phys. Rev. B* **9**, 600 (1974).
- ³⁵P. D. C. King, T. D. Veal, C. F. McConville, F. Fuchs, J. Furthmüller, F. Bechstedt, J. Schörmann, D. J. As, K. Lischka, H. Lu, and W. J. Schaff, *Phys. Rev. B* **77**, 115213 (2008).
- ³⁶P. D. C. King, T. D. Veal, A. Schleife, J. Zúñiga-Pérez, B. Martel, P. H. Jefferson, F. Fuchs, V. Muñoz-Sanjosé, F. Bechstedt, and C. F. McConville, *Phys. Rev. B* **79**, 205205 (2009).
- ³⁷S.-H. Wei and A. Zunger, *Phys. Rev. B* **37**, 8958 (1988).
- ³⁸C. Persson and A. Zunger, *Phys. Rev. B* **68**, 073205 (2003).
- ³⁹F. Fuchs, J. Furthmüller, F. Bechstedt, M. Shishkin, and G. Kresse, *Phys. Rev. B* **76**, 115109 (2007).
- ⁴⁰J. J. Yeh and I. Lindau, *At. Data Nucl. Data Tables* **32**, 1 (1985).
- ⁴¹M. B. Trzhaskovskaya, V. I. Nefedov, and V. G. Yarzhevsky, *At.*

- Data Nucl. Data Tables **77**, 97 (2001).
- ⁴²H. L. Zhang, D. J. Payne, R. G. Palgrave, V. Lazarov, A. T. S. Wee, W. Chen, C. F. McConville, P. D. C. King, T. D. Veal, G. Panaccione, P. Lacovig, and R. G. Egdell (unpublished).
- ⁴³S. A. Chambers, T. Droubay, T. C. Kaspar, and M. Gutowski, J. Vac. Sci. Technol. B **22**, 2205 (2004).
- ⁴⁴P. D. C. King, T. D. Veal, and C. F. McConville, Phys. Rev. B **77**, 125305 (2008).
- ⁴⁵G. Paasch and H. Übensee, Phys. Status Solidi B **113**, 165 (1982).
- ⁴⁶J.-P. Zöllner, H. Übensee, G. Paasch, T. Fiedler, and G. Gobsch, Phys. Status Solidi B **134**, 837 (1986).
- ⁴⁷A. Schleife, F. Fuchs, C. Rödl, J. Furthmüller, and F. Bechstedt, Appl. Phys. Lett. **94**, 012104 (2009).